NANO LETTERS

pubs.acs.org/NanoLett Letter

Nanocapillarity and Nanoconfinement Effects of Pipet-like Bismuth@Carbon Nanotubes for Highly Efficient Electrocatalytic CO_2 Reduction

Wenjun Zhang, Songyuan Yang, Minghang Jiang, Yi Hu, Chaoquan Hu,* Xiaoli Zhang, and Zhong Jin*

Cite This: *Nano Lett.* 2021, 21, 2650−2657 Read Online

ACCESS | Metrics & More | Article Recommendations | Supporting Information

ABSTRACT: Electrocatalytic CO_2 reduction reaction is regarded as an intriguing route for producing renewable chemicals and fuels, but its development is limited by the lack of highly efficient and stable electrocatalysts. Herein, we propose the pipet-like bismuth (Bi) nanorods semifilled in nitrogen-doped carbon nanotubes (Bi-NRs@NCNTs) for highly selective electrocatalytic CO_2 reduction. Benefited from the prominent capillary and confinement effects, the Bi-NRs@NCNTs act as nanoscale conveyors that can significantly facilitate the mass transport, adsorption,and concentration of reactants onto the active sites, realizing rapid reaction kinetics and low cathodic polarization. The spatial encapsulation and separation by the NCNT shells prevents the self-aggregation and surface oxidation of Bi-NRs, increasing the dispersity and stability of the electrocatalyst. As a result, the Bi-NRs@NCNTs exhibit high activity and durable catalytic stability for CO_2-to-formate conversion over a wide potential range. The Faradaic efficiency for formate production reaches 90.9% at a moderate applied potential of −0.9 V vs reversible hydrogen electrode (RHE).

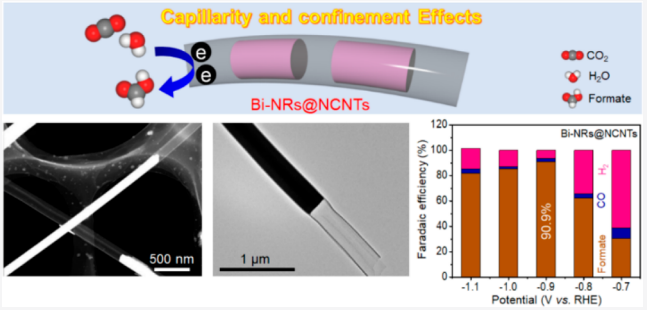

KEYWORDS: *electrochemical CO_2 reduction, formate production, selectivity, nanocapillarity, nanoconfinement*

INTRODUCTION

In the past decades, the issues of greenhouse effect and global warming have deteriorated due to the increased CO_2 emissions. Gaseous CO_2 can be converted into carbohydrates through the natural photosynthesis process in plants, but the energy conversion efficiency is relatively low (normally less than 2%).[1,2] The design of bioinspired artificial photosynthesis systems has attracted wide attention.[3] Especially, electrocatalytic CO_2 reduction reaction (CO_2RR) has been regarded as a promising strategy for converting CO_2 to value-added carbonaceous chemicals or renewable fuels via moderate reaction routes.[4−6] Formate, as a typical liquid-phase product of CO_2RR, can be used in formate fuel cells as the hydrogen carrier with the merits of easy/safe transportation and storage.[7,8] However, the activation and reduction of CO_2 molecule is difficult due to its thermodynamically stable traits.[9,10] Suffering from the high energy barriers for CO_2 activation and intermediate absorption/adsorption, the development of the electrocatalytic CO_2RR process is restricted by the large overpotential, low catalytic efficiency, and competing hydrogen evolution reaction (HER).[11−13]

Among the candidates of earth abundant electrocatalysts for CO_2-to-formate production, Sn, Co, and Cu based materials[14−20] have attracted extensive attention due to the preferable *OCHO formation and weak *HCOOH binding capability toward formate formation, but with the limitation of inferior selectivity, stability, or excess overpotentials. Bismuth (Bi) based electrocatalysts have been considered as an alternative choice for CO_2RR, exhibiting high free energy for hydrogen adsorption that can effectively suppress the HER.[21−23] Numerous studies on metallic Bi were focused on its CO_2RR activity in ionic liquids with CO as the major product,[24−27] but its application in aqueous solution is limited by the high overpotential and low durability. To address this problem, it is rewarding to fabricate Bi-based electrocatalysts at the nanoscale, such as constructing different Bi nanostructures (e.g., nanowires, nanorods, and nanosheets[28−31]) with high electrochemical surface area (ECSA) and abundant active sites.

To further improve the electrocatalytic performances of Bi-based materials for CO_2RR, we suggest that further combining Bi nanostructures with carbon nanomaterials to form a rationally constructed composite matrix and interface will be very helpful to enhance the conductivity and cycle stability. Herein, a pipet-like composite of Bi nanorods semifilled in

Received: January 31, 2021
Revised: February 22, 2021
Published: March 12, 2021

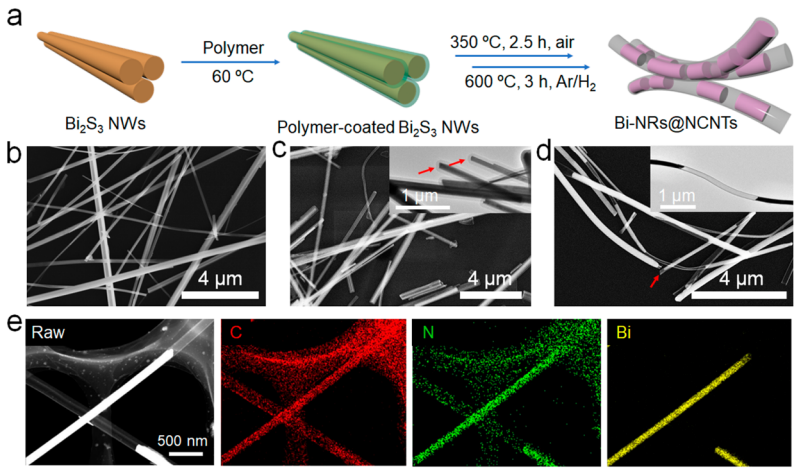

Figure 1. (a) Schematic illustration of the synthetic process of Bi-NRs@NCNTs. (b–d) SEM images of (b) precursor Bi_2S_3 NWs, (c) polymer-coated Bi_2S_3 NWs, and (d) Bi-NRs@NCNTs. (e) SEM image and corresponding EDX elemental mappings of Bi-NRs@NCNTs. The insets in (c) and (d) are the TEM images of polymer-coated Bi_2S_3 NWs and Bi-NRs@NCNTs, respectively.

nitrogen-doped carbon nanotubes (Bi-NRs@NCNTs) is demonstrated as a high-performance electrocatalyst with significant nanocapillary and nanoconfinement effects for boosting CO_2-to-formate conversion. The metallic Bi nanorods with low *OCHO formation energy and *HCOOH binding energy are conducive to highly selective CO_2-to-formate conversion. Owing to the high-aspect-ratio structure, the Bi-NRs@NCNTs exhibit enhanced electronic conductivity and surface contact ability, thus lowering the cathodic polarization. The spatial restriction by NCNT shells can efficiently prevent the self-aggregation and surface oxidation of Bi nanorods, efficiently maintaining the catalytic activity and durability. Moreover, the capillarity and confinement effects of Bi-NRs@NCNTs significantly enhance the transport, adsorption, and concentration of the reactants and reaction intermediates, leading to a rapid reaction rate. As a result, the Bi-NRs@NCNTs achieve a high Faradaic efficiency for formate production (90.9% $FE_{Formate}$) with a current density of 6.0 mA cm^{-2} at a moderate potential (−0.9 V vs reversible hydrogen electrode, RHE) in an aqueous solution as well as long-term stability for CO_2RR.

RESULTS AND DISCUSSION

The Bi-NRs@NCNTs were synthesized via the coating of a polymer layer on Bi_2S_3 nanowires (Bi_2S_3 NWs) and the subsequent thermal treatment processes, as illustrated in Figure 1a. The Bi_2S_3 NWs with the average diameter of ∼300 nm and the lengths up to several millimeters were prepared via a convenient solvothermal method (Figure 1b). Then, the polymerization of L-cysteine, resorcinol, formaldehydes, and ammonia hydroxide were in situ triggered on the surface of Bi_2S_3 NWs, leading to the formation of polymer-coated Bi_2S_3 NWs (Figure 1c). The polymer-coated Bi_2S_3 NWs were thermally treated to realize the reduction of Bi_2S_3 NWs into Bi-NRs and the carbonization of the polymer layer into NCNTs, finally forming core–shell nanostructured Bi-NR@NCNTs (Figure 1d). Compared with precursor Bi_2S_3 NWs, the Bi-NRs encapsulated in NCNT shells are randomly separated and shrunken in volume due to the Rayleigh instability effect (details in Figure S1).[32] Scanning electron microscopy (SEM) confirms that the pipet-like Bi-NR@NCNTs have large internal cavities and void space. Energy-dispersive X-ray spectroscopy (EDX) elemental mappings of Bi-NRs@NCNTs were collected (Figure 1e). The outer NCNT shells show a homogeneous distribution of C and N elements, and the inner Bi-NRs show evenly distributed Bi species. Moreover, the complete removal of the S element is confirmed by the EDX spectrum (Figure S2).

Transmission electron microscopy (TEM) images show that the as-produced Bi-NRs possess a smaller diameter than the precursor Bi_2S_3 NW, and the inner void space exists between two separated Bi-NRs (the insets in Figure 1c,d). As shown in Figure 2a,b, the Bi-NRs have a diameter of ∼247.0 nm and the

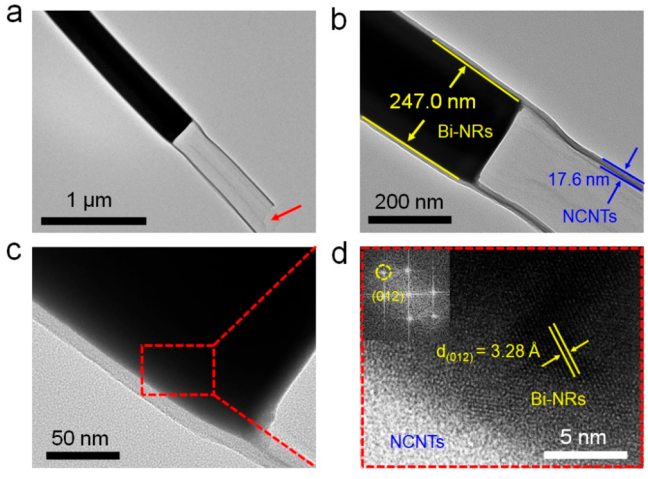

Figure 2. (a–d) TEM and HRTEM images of Bi-NRs@NCNTs at different magnification degrees. The corresponding SAED pattern in the inset of (d) reveals the high crystalline feature of metallic Bi.

NCNT layer possesses a thickness of ∼17.6 nm. The high-resolution TEM (HRTEM) images (Figure 2c) display that the Bi-NRs@NCNTs are composed of outer NCNT shells and inner cores of highly crystalline Bi-NRs. The HRTEM image (Figure 2d) and the corresponding SAED pattern (the inset of Figure 2d) measured on the core Bi-NRs of Bi-NRs@NCNTs show a lattice spacing of 0.328 nm, which is assigned to the (012) planes of metallic Bi, indicating the high crystalline nature.

https://dx.doi.org/10.1021/acs.nanolett.1c00390
Nano Lett. 2021, 21, 2650−2657

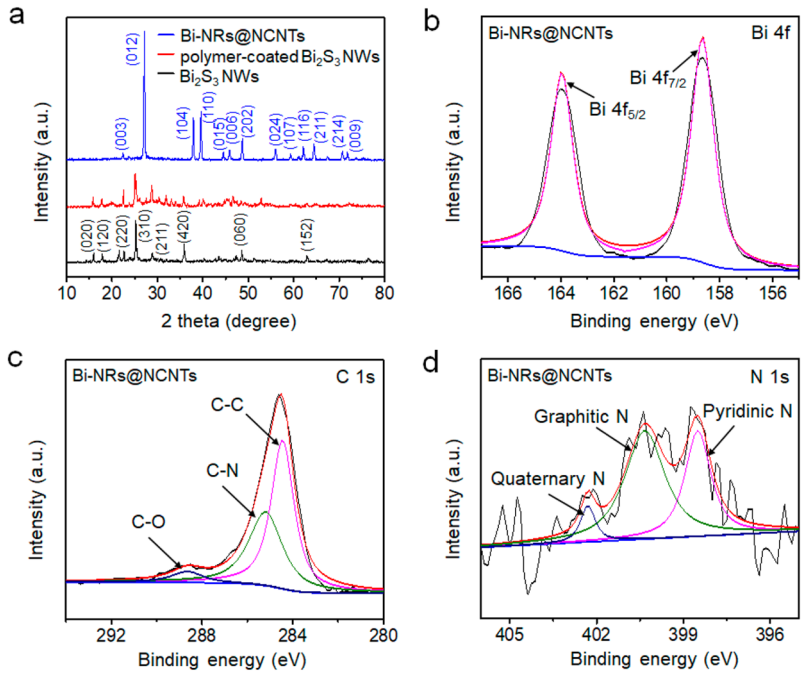

Figure 3. (a) XRD patterns of precursor Bi_2S_3 NWs, polymer-coated Bi_2S_3 NWs, and Bi-NRs@NCNTs. (b–d) XPS spectra of the (b) Bi 4f, (c) C 1s, and (d) N 1s regions of Bi-NRs@NCNTs.

X-ray diffraction (XRD) and Raman and X-ray photoelectron spectroscopy (XPS) techniques were used to analyze the compositions and crystalline structures of Bi-NRs@NCNTs. As shown in Figure 3a, the precursor Bi_2S_3 NWs were first synthesized, and all the XRD peaks (black line) are perfectly assigned to the orthorhombic Bi_2S_3, which are consistent with the standard data (JCPDS No. 17-0320), indicating the high purity of the precursor Bi_2S_3 NWs. Then, the polymer-coated Bi_2S_3 NWs were obtained, and most of the XRD peaks (red line) matched well with the orthorhombic Bi_2S_3, while the remaining peaks were assigned to the resin shell. Finally, the polymer-coated Bi_2S_3 NWs were transformed into Bi-NRs@NCNTs. The XRD peaks of Bi-NRs@NCNTs (navy blue line) were well indexed to rhombohedral Bi (JCPDS No. 44-1246), and no indication of oxidized Bi components was detected; meanwhile, the broad diffraction peak of the outer NCNT shells indicated the partially graphitic nature. The presence of NCNTs is further confirmed by a Raman spectrum (Figure S3a). The Raman peaks centered at 1345.5 cm^{-1} (D band) and 1592.3 cm^{-1} (G band) are assigned to the characteristic peaks of carbon material, and moreover, the value of i_D/i_G in the Raman spectrum is calculated to be 0.87, further confirming the partially graphitic feature of the NCNTs. The elemental compositions of Bi-NRs@NCNTs were further detected by XPS. The main peaks of Bi $4f_{5/2}$ (164.0 eV) and Bi $4f_{7/2}$ (158.6 eV) are assigned to Bi(0)[33] and further verify the presence of metallic Bi (Figure 3b). The three peaks located in the C 1s region are indexed to the characteristic peaks of C–C, C–N, and C–O bonds (Figure 3c),[33] respectively, which further confirm the presence of NCNT shells. The appearance of the N 1s peak proves the N element has been doped in carbon nanotubes since L-cysteine and ammonia hydroxide were used as precursors to synthesize the polymer layer that covered the Bi_2S_3 NWs. The XPS spectrum in the N 1s region presented three main peaks, corresponding to graphitic N, pyridinic N, and quaternary N,[33] respectively (Figure 3d). The atomic contents of the C, N, and Bi species in Bi-NRs@NCNTs are measured to be 80.3%, 4.1%, and 15.6%, respectively. The synergistic effects of the conductive carbon layer and N heteroatom doping can improve the electron transfer and bring abundant electron-rich defects/active centers, which also benefits the electrochemical activity of Bi-NRs@NCNTs. Meanwhile, N dopants can adjust the electronic structures of Bi-NRs@NCNTs to optimize the adsorption capacities of the reaction intermediate and thus facilitates the catalytic kinetics.[34] The N_2 adsorption–desorption isotherms reveal the specific surface area of Bi-NRs@NCNTs (10.6 m^2 g^{-1}) via the Brunauer–Emmett–Teller (BET) method (Figure S3b). The as-calculated pore-size distribution indicates the presence of mesopores and cavities on the surface of the Bi-NRs@NCNTs (Figure S3c), which can enhance the reaction kinetics and improve the product selectivity toward CO_2RR. The reasons are listed as follows. First, the mesopores and cavities can provide an abundant curved internal surface, which not only increases the density of the active centers or undercoordinated sites to facilitate the rapid transport of reactants but also realizes the improved binding ability of the reactants and intermediates.[35] Second, an appropriately designed mesoporous structure can take full advantage of the transport characteristics of the reaction species. Especially, during the CO_2RR, the mesopores can bring about the effect of the diffusion gradients, which effectively suppresses the competing HER driven by the increased alkalinity that developed within the mesoporous network. In comparison, CO_2 reduction is able to be more resistant to the transport limitations than HER and thereby facilitate the CO_2 conversion efficiency. For better comparison, Bi granules (Figure S4) and pristine NCNTs (Figures S5 and S6) as two control samples were also prepared, as detailed in the Experimental Section. As confirmed by the CO_2 adsorption isotherms at 273 K (Figure S 3d), the Bi-NRs@NCNTs exhibit a larger CO_2 uptake capacity than that of the Bi

https://dx.doi.org/10.1021/acs.nanolett.1c00390
Nano Lett. 2021, 21, 2650–2657

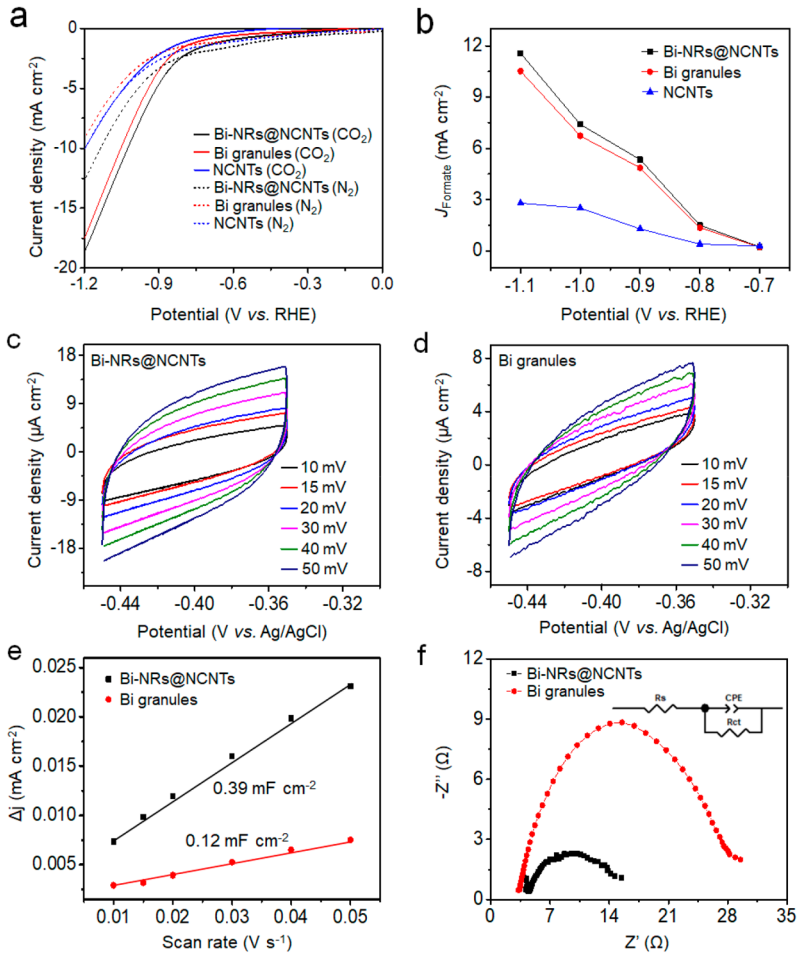

Figure 4. (a) LSV curves of Bi-NRs@NCNTs, Bi granules, and pristine NCNTs measured in CO_2- or N_2-saturated 0.1 M $KHCO_3$ aqueous solution, respectively. (b) The calculated $J_{Formate}$ values of Bi-NRs@NCNTs, Bi granules, and NCNTs. (c, d) The CV curves of (c) Bi-NRs@NCNTs and (d) Bi granules measured in N_2-saturated 0.1 M $KHCO_3$ aqueous solution. (e) The plots of charging current density differences (Δj) vs scan rates and (f) the Nyquist plots of Bi-NRs@NCNTs and Bi granules, respectively. The inset in (f) is the magnified Nyquist plots of Bi-NRs@NCNTs and Bi granules at low frequency.

granules, which lays the foundation of pipet-like Bi-NRs@NCNTs for enhanced CO_2 adsorption and furthering the CO_2RR process.

The electrocatalytic activities of Bi-NRs@NCNTs, Bi granules, and pristine NCNTs toward CO_2RR were evaluated in 0.1 M $KHCO_3$ aqueous solution. To evaluate the influence of competing HER as a possible side reaction, linear sweep voltammetry (LSV) curves of these samples were measured in CO_2- and N_2-purged 0.1 M $KHCO_3$ aqueous solution, respectively (Figure 4a). The Bi-NRs@NCNTs show much higher current density in a CO_2-saturated electrolyte than that in the N_2 atmosphere, indicating that the Bi-NRs@NCNTs could exhibit a high selectivity for CO_2RR rather than HER. In contrast, Bi granules and pristine NCNTs show lower current densities in CO_2-saturated electrolyte than that of Bi-NRs@NCNTs, indicating their lower activity. Meanwhile, the current densities of pristine NCNTs measured in CO_2- and N_2-saturated electrolytes show a nonsignificant difference over the whole potential range, indicating the occurrence of a competing HER process. The Bi-NRs@NCNTs show higher current densities for formate production ($J_{Formate}$) when compared with Bi granules (Figure 4b). The differences in electrocatalytic activities between Bi-NRs@NCNTs and Bi granules are also compared by the ECSA measured from cyclic voltammetry (CV) tests (Figure 4c,d) and the corresponding curves of charging current density differences (Δj) vs scan rates (Figure 4e). The ECSA shows a 3-fold increase from micrometer-sized Bi granules to Bi-NRs@NCNTs, suggesting that the nanocapillarity and nanoconfinement effects of Bi-NRs@NCNTs makes an important contribution to provide more catalytically active sites for the enhanced CO_2RR activity.[17] Moreover, as displayed in the Nyquist plots and the corresponding equivalent circuit measured by electrochemical impedance spectroscopy (EIS) analysis (Figure 4f), the interfacial electron transfer resistance (R_{ct}) value of Bi-NRs@NCNTs (12.0 Ω) is much smaller than that of Bi granules (25.2 Ω), which can facilitate the occurrence of electrocatalytic CO_2RR.

The current densities of Bi-NRs@NCNTs, Bi granules, and pristine NCNTs for electrochemical CO_2RR have been measured and summarized, as shown in Figure 5a−c. The current density is expected to be increased when the applied potential becomes more negative. When compared with Bi-NRs@NCNTs, the current density of pristine NCNTs never exceeds 10 mA cm^{-1} until the applied potential is tuned down to −1.2 V vs RHE. This phenomenon indicates that metallic Bi plays a significant role to enhance the electrocatalytic performance. In contrast, the Bi-NRs@NCNTs show higher

https://dx.doi.org/10.1021/acs.nanolett.1c00390
Nano Lett. 2021, 21, 2650−2657

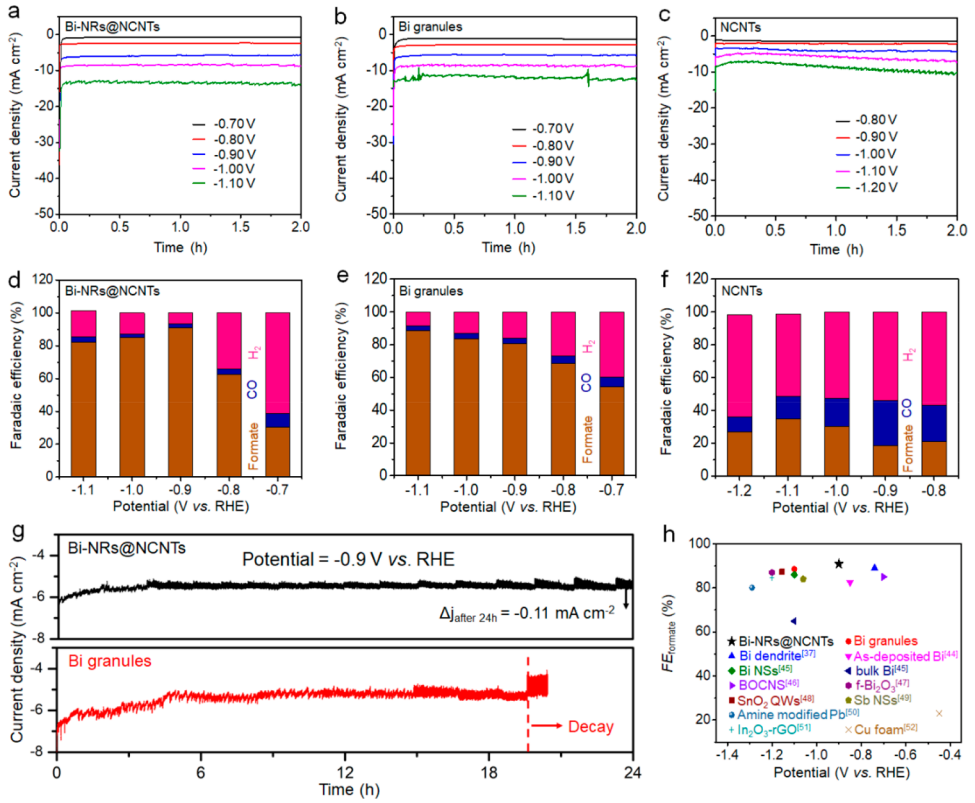

Figure 5. (a–c) Time-dependent current density curves of (a) Bi-NRs@NCNTs, (b) Bi granules, and (c) pristine NCNTs at different potentials. (d–f) Faradaic efficiencies of the reduction products generated by (d) Bi-NRs@NCNTs, (e) Bi granules, and (f) pristine NCNTs after CO_2RR tests for 2 h at different potentials. (a) Capillary phenomenon of Bi-NRs@NCNTs played in CO_2RR for the enhanced reactant transport. (b) Contact angle test of the $KHCO_3$ aqueous solution on the Bi-NRs@NCNTs surface. (g) Long-term CO_2RR tests of Bi-NRs@NCNTs and Bi granules for 24 h. (h) Comparisons of $FE_{Formate}$ for Bi-NRs@NCNTs with other electrocatalysts reported in the previous literature.[37,44−52]

overall current density values than that of Bi granules. To divide the contributions from the CO_2RR and the HER to the overall current density, we further quantify the species and amounts of individual reduction products (H_2 and carbonaceous compounds) at the selected potentials to evaluate the accurate activity and selectivity of these catalysts toward CO_2RR. In virtue of the gas chromatograph (GC) and nuclear magnetic resonance (NMR) analysis, the main products generated by the above samples are measured to be formate, CO, and H_2, and the corresponding yield rates of these products at different applied potentials are provided in Figure S7. As shown in Figure 5d, the Bi-NRs@NCNTs tend to yield formate as the predominant CO_2RR product, while the generation of CO and H_2 is also detected and the amounts are varied at different potentials. At −0.7 V vs RHE, $FE_{Formate}$ is only approximately 30%, together with the Faradaic efficiency for H_2 production (FE_{H2}) reaching above 50%, owing to the competing side reaction of HER. When the applied potential changes to −0.8 and −0.9 V vs RHE, $FE_{Formate}$ is significantly increased. $FE_{Formate}$ reaches a peak value of 90.9% at −0.9 V vs RHE, associated with a stable current density of 6.0 mA cm^{-1}. When the given potential becomes more negative, $FE_{Formate}$ begins to decrease slowly since the mass transfer and supply of reactant CO_2 molecules undergo a diffusion-limited process at a larger current density, rather than the intrinsic activity limitation of the catalyst itself. Moreover, FE_{H2} is still suppressed to small values (<15%) when the applied potential becomes more negative and finally reaches −1.1 V vs RHE. This result confirms that the Bi-NRs@NCNTs possess a high selectivity for formate production, and importantly, $FE_{Formate}$ can be maintained at a high level over a broad potential range. In contrast, as shown in Figure 5e, the Bi granules exhibit $FE_{Formate}$ values relatively lower than those of Bi-NRs@NCNTs at the potentials between −0.7 and −1.0 V vs RHE. The Bi granules show a peak $FE_{Formate}$ value of 88.5% until the potential finally reaches −1.1 V vs RHE, which require a much higher overpotential than the Bi-NRs@NCNTs.

We also have conducted the same control experiments by using a commercial Bi powder with a bulk morphology (Figure S8a,b). The of Bi powder only achieves $FE_{Formate}$ values of 79.8% and 84.6% at −1.0 and −1.1 V vs RHE, respectively (Figure S8c,d), which are much inferior than those of as-synthesized Bi-NRs@NCNTs. In addition, when using the pristine NCNTs (after the removal of Bi-NRs) as the electrocatalyst (Figure S5), the main reduction product is found to be H_2, and the selectivity for formate generation is much inferior (Figure 5f). The FE_{H2} of pristine NCNTs is retained at higher than 50% at a broad potential range from −0.8 V to −1.2 V vs RHE. For pristine NCNTs, the current densities are lower, and the HER acts as a significant competing reaction when compared with the Bi-containing samples.

The above experimental results confirm that the Bi-NRs@NCNTs possess a high activity and selectivity for CO_2RR, which benefits from the vital functions of inner metallic Bi-NR cores that can lower the *OCHO formation energy and *HCOOH binding energy toward a preferable CO_2-to-formate conversion pathway.[32,36] Especially, the exposed high-index

https://dx.doi.org/10.1021/acs.nanolett.1c00390
Nano Lett. 2021, 21, 2650−2657

(012) planes of Bi-NRs (Figure 2d) can serve as a better catalytic active site to significantly lower the activation barriers for the element steps of the CO_2-to-formate conversion pathway,

$$* + CO_2 + [H^+ + e^-] \rightarrow *OCHO \quad (1)$$

$$*OCHO + [H^+ + e^-] \rightarrow *HCOOH \quad (2)$$

thus, contributing to preferable formate production over other CO_2RR products.[37] Moreover, the strong nanocapillary effect of tubular nanostructures also plays an important role, which has been observed by previous studies[38−42] on the enhanced liquid transport in carbon nanotubes; detailed descriptions are in Figure S9. Furthermore, owing to the nanoconfinement effect of hollow Bi-NRs@NCNTs,[43] the reactant molecules can bind more strongly on the interior surface of the NCNTs, and the trapping of the reaction intermediates inside such nanochannels could strengthen their contact with active sites, thus increasing the reduction rate of CO_2 as well as the yields of the CO_2RR products. One the other hand, the one-dimensional (1D) NCNT shells can efficiently prevent the self-aggregation of adjacent Bi-NRs, since the encapsulation in such nanosized channels can provide effective spatial separation for Bi-NRs. Meanwhile, the protection of NCNT shells could prevent the surface oxidation of metallic Bi and suppress the deactivation of the electrocatalyst.

To evaluate the performance and structural stability of Bi-NRs@NCNTs, a long-term CO_2RR test was conducted in CO_2-saturated a 0.1 M $KHCO_3$ aqueous solution (Figure 5g). During the electrolysis for 24 h at the potential of −0.9 V vs RHE, the activity of Bi-NRs@NCNTs shows no obvious change over the entire process and the current density only decreases by 0.11 mA cm^{-1}. The periodic fluctuations of the current density are attributed to the generation, absorption, and desorption of gas products on the surface of electrodes when gaseous CO_2 is continuously purged into a cathodic compartment with a flow rate of 20 mL min^{-1}. The possible morphology and structure variations of Bi-NRs@NCNTs have been analyzed by SEM, TEM, XRD, and XPS after the long-term CO_2RR test (Figures S10 and S11). These characterizations verify the good structural integrity and unchanged elemental compositions of Bi-NRs@NCNTs, proving the high stability during the electrocatalytic process. Meanwhile, the crystalline structure and valence state of metallic Bi(0) are well maintained. In contrast, Bi granules exhibit an inferior stability during the entire course of bulk electrolysis (Figure 5g). The current density continuously decreases and then declines sharply at the 21st hour, indicating an obvious activity decay. These results indicate that the outer NCNT shells of Bi-NRs@NCNTs not only provide a favorable capillary effect and nanoconfined space for facilitating CO_2RR but also protect the inner Bi-NRs from degradation during long-term electrolytic operation. For further comparison, we have summarized the CO_2-to-formate conversion performances of Bi-NRs@NCNTs with other representative electrocatalysts reported in previous literature (Figure 5h and Table S1).[37,44−52] It suggests that the Bi-NRs@NCNTs in this work exhibit competitive activity and selectivity for CO_2RR toward formate production.

CONCLUSIONS

In summary, we report the use of a pipet-like Bi-NRs@NCNTs catalyst with encapsulated Bi-NRs semifilled in NCNT shells induced by Rayleigh instability. The 1D pipet-like nanostructure of Bi-NRs@NCNTs can enlarge the ECSA and facilitate electron transfer, effectively lowering the *OCHO formation energy and *HCOOH binding energy for highly selective CO_2-to-formate conversion. Meanwhile, the favorable nanocapillary and nanoconfinement effects synergistically facilitate the mass transfer, adsorption, and concentration of reactant CO_2 molecules onto the active sites, which promotes the reaction rate and decreases the overpotential. The encapsulation and spatial separation by NCNT shells effectively prevents the Bi-NRs from self-aggregation and surface oxidation during the CO_2RR process, ensuring the structural integrity and performance stability of the electrolyte. Benefiting from the above merits, the Bi-NRs@NCNTs exhibit a high selectivity (90.9%) and stability for CO_2-to-formate conversion at a modest applied potential (−0.9 V vs RHE). This work presents a promising strategy to construct environmentally friendly and low-cost electrocatalysts with a proper nanoconfined structure and protective matrix for high-efficient electrocatalytic CO_2RR systems.

ASSOCIATED CONTENT

Supporting Information

The Supporting Information is available free of charge at https://pubs.acs.org/doi/10.1021/acs.nanolett.1c00390.

Experimental methods, figures showing additional characterization data, and table showing performance comparisons (PDF)

AUTHOR INFORMATION

Corresponding Authors

Chaoquan Hu − *State Key Laboratory of Multiphase Complex Systems, Institute of Process Engineering, Chinese Academy of Sciences, Beijing 100190, China*; Email: cqhu@ipe.ac.cn

Zhong Jin − *MOE Key Laboratory of Mesoscopic Chemistry, MOE Key Laboratory of High Performance Polymer Materials and Technology, Jiangsu Key Laboratory of Advanced Organic Materials, School of Chemistry and Chemical Engineering, Nanjing University, Nanjing 210023, China; Shenzhen Research Institute of Nanjing University, Shenzhen 518063, China*; orcid.org/0000-0001-8860-8579; Email: zhongjin@nju.edu.cn

Authors

Wenjun Zhang − *MOE Key Laboratory of Mesoscopic Chemistry, MOE Key Laboratory of High Performance Polymer Materials and Technology, Jiangsu Key Laboratory of Advanced Organic Materials, School of Chemistry and Chemical Engineering, Nanjing University, Nanjing 210023, China; Jiangsu Co-Innovation Center of Efficient Processing and Utilization of Forest Resources, Jiangsu Province Key Laboratory of Green Biomass-based Fuels and Chemicals, College of Chemical Engineering, Nanjing Forestry University, Nanjing 210037, China; Shenzhen Research Institute of Nanjing University, Shenzhen 518063, China*

Songyuan Yang − *MOE Key Laboratory of Mesoscopic Chemistry, MOE Key Laboratory of High Performance Polymer Materials and Technology, Jiangsu Key Laboratory of Advanced Organic Materials, School of Chemistry and Chemical Engineering, Nanjing University, Nanjing 210023, China; Shenzhen Research Institute of Nanjing University, Shenzhen 518063, China*

https://dx.doi.org/10.1021/acs.nanolett.1c00390
Nano Lett. 2021, 21, 2650−2657

Minghang Jiang − *MOE Key Laboratory of Mesoscopic Chemistry, MOE Key Laboratory of High Performance Polymer Materials and Technology, Jiangsu Key Laboratory of Advanced Organic Materials, School of Chemistry and Chemical Engineering, Nanjing University, Nanjing 210023, China; Shenzhen Research Institute of Nanjing University, Shenzhen 518063, China*

Yi Hu − *MOE Key Laboratory of Mesoscopic Chemistry, MOE Key Laboratory of High Performance Polymer Materials and Technology, Jiangsu Key Laboratory of Advanced Organic Materials, School of Chemistry and Chemical Engineering, Nanjing University, Nanjing 210023, China; Shenzhen Research Institute of Nanjing University, Shenzhen 518063, China*

Xiaoli Zhang − *School of Materials Science and Engineering, Zhengzhou University, Zhengzhou 450001, China*

Complete contact information is available at: https://pubs.acs.org/10.1021/acs.nanolett.1c00390

Notes

The authors declare no competing financial interest.

■ ACKNOWLEDGMENTS

This work was supported by the National Key Research and Development Program of China (2017YFA0208200), the Fundamental Research Funds for the Central Universities of China (0205-14380219, 0205-14913212), the Projects of NSFC (22022505, 21872069, 51761135104), the Natural Science Foundation of Jiangsu Province (BK20180008), and the Shenzhen Fundamental Research Program of Science, Technology and Innovation Commission of Shenzhen Municipality (JCYJ20180307155007589).

■ REFERENCES

(1) Dogutan, D. K.; Nocera, D. G. Artificial photosynthesis as efficiencies greatly exceeding that of natural photosynthesis. *Acc. Chem. Res.* **2019**, *52*, 3143−3148.

(2) Nocera, D. G. The artificial leaf. *Acc. Chem. Res.* **2012**, *45*, 767−776.

(3) Hepburn, C.; Adlen, E.; Beddington, J.; Carter, E. A.; Fuss, S.; Mac Dowell, N.; Minx, J. C.; Smith, P.; Williams, C. K. The technological and economic prospects for CO_2 utilization and removal. *Nature* **2019**, *575*, 87−97.

(4) Yaashikaa, P. R.; Senthil Kumar, P.; Varjani, S. J.; Saravanan, A. A review on photochemical, biochemical and electrochemical transformation of CO_2 into value-added products. *J. CO2 Utilization* **2019**, *33*, 131−147.

(5) Kibria, M. G.; Edwards, J. P.; Gabardo, C. M.; Dinh, C. T.; Seifitokaldani, A.; Sinton, D.; Sargent, E. H. Electrochemical CO_2 reduction into chemical feedstocks: from mechanistic electrocatalysis models to system design. *Adv. Mater.* **2019**, *31*, 1807166.

(6) Martín, A. J.; Pérez-Ramírez, J. Heading to distributed electrocatalytic conversion of small abundant molecules into fuels, chemicals, and fertilizers. *Joule* **2019**, *3*, 2602−2621.

(7) Grubel, K.; Jeong, H.; Yoon, C. W.; Autrey, T. Challenges and opportunities for using formate to store, transport, and use hydrogen. *J. Energy Chem.* **2020**, *41*, 216−224.

(8) An, L.; Chen, R. Direct formate fuel cells: A review. *J. Power Sources* **2016**, *320*, 127−139.

(9) Birdja, Y. Y.; Perez-Gallent, E.; Figueiredo, M. C.; Gottle, A. J.; Calle-Vallejo, F.; Koper, M. T. M. Advances and challenges in understanding the electrocatalytic conversion of carbon dioxide to fuels. *Nat. Energy* **2019**, *4*, 732−745.

(10) Zhang, W. J.; Hu, Y.; Ma, L. B.; Zhu, G. Y.; Wang, Y. R.; Xue, X. L.; Chen, R. P.; Yang, S. Y.; Jin, Z. Progress and perspective of electrocatalytic CO_2 reduction for renewable carbonaceous fuels and chemicals. *Adv. Sci.* **2018**, *5*, 1700275.

(11) Lee, C. W.; Cho, N. H.; Im, S. W.; Jee, M. S.; Hwang, Y. J.; Min, B. K.; Nam, K. T. New Challenges of electrokinetic studies in investigating the reaction mechanism of electrochemical CO_2 reduction. *J. Mater. Chem. A* **2018**, *6*, 14043−14057.

(12) Kas, R.; Ayemoba, O.; Firet, N. J.; Middelkoop, J.; Smith, W. A.; Cuesta, A. In-situ infrared spectroscopy applied to the study of the electrocatalytic reduction of CO_2: theory, practice and challenges. *ChemPhysChem* **2019**, *20*, 2904−2925.

(13) Geng, Z. G.; Kong, X. D.; Li, Q. Y.; Ke, J. W.; Zeng, J. Engineering electronic structures of nanomaterials toward carbon dioxide electroreduction. *Current Opinion in Electro.* **2019**, *17*, 7−15.

(14) Chen, Z.; Fan, T. T.; Zhang, Y. Q.; Xiao, J.; Gao, M. R.; Duan, N. Q.; Zhang, J. W.; Li, J. H.; Liu, Q. X.; Yi, X. D.; Luo, J. L. Wavy SnO_2 catalyzed simultaneous reinforcement of carbon dioxide adsorption and activation towards electrochemical conversion of CO_2 to HCOOH. *Appl. Catal., B* **2020**, *261*, 118243.

(15) Liu, G. B.; Li, Z. H.; Shi, J. J.; Sun, K.; Ji, Y. J.; Wang, Z. G.; Qiu, Y. F.; Liu, Y. Y.; Wang, Z. J.; Hu, P. A. Black reduced porous SnO_2 nanosheets for CO_2 electroreduction with high formate selectivity and low overpotential. *Appl. Catal., B* **2020**, *260*, 118134.

(16) Gao, S.; Sun, Z. T.; Liu, W.; Jiao, X. C.; Zu, X. L.; Hu, Q.; Sun, Y. F.; Yao, T.; Zhang, W. H.; Wei, S. Q.; Xie, Y. Atomic layer confined vacancies for atomic-level insights into carbon dioxide electroreduction. *Nat. Commun.* **2017**, *8*, 14503.

(17) Gao, S.; Lin, Y.; Jiao, X. C.; Sun, Y. F.; Luo, Q. Q.; Zhang, W. H.; Li, D. Q.; Yang, J. L.; Xie, Y. Partially oxidized atomic cobalt layers for carbon dioxide electroreduction to liquid fuel. *Nature* **2016**, *529*, 68−71.

(18) Shen, S. B.; He, J.; Peng, X. Y.; Xi, W.; Zhang, L. H.; Xi, D. S.; Wang, L.; Liu, X. J.; Luo, J. Stepped surface-rich copper fiber felt as an efficient electrocatalyst for the CO_2RR to formate. *J. Mater. Chem. A* **2018**, *6*, 18960−18966.

(19) Yoon, S. H.; Kang, U.; Park, H.; Abdel-Wahab, A.; Han, D. S. Computational density functional theory study on the selective conversion of CO_2 to formate on homogeneously and heterogeneously mixed $CuFeO_2$ and CuO surfaces. *Catal. Today* **2019**, *335*, 345−353.

(20) Vasileff, A.; Zhi, X.; Xu, C. C.; Ge, L.; Jiao, Y.; Zheng, Y.; Qiao, S.-Z. Selectivity control for electrochemical CO_2 reduction by charge redistribution on the surface of copper alloys. *ACS Catal.* **2019**, *9*, 9411−9417.

(21) Greeley, J.; Jaramillo, T. F.; Bonde, J.; Chorkendorff, I.; Nørskov, J. K. Computational high-throughput screening of electrocatalytic materials for hydrogen evolution. *Nat. Mater.* **2006**, *5*, 909−913.

(22) Wu, M. G.; Xu, B. L.; Zhang, Y. F.; Qi, S. H.; Ni, W.; Hu, J.; Ma, J. M. Perspectives in emerging bismuth electrochemistry. *Chem. Eng. J.* **2020**, *381*, 122558.

(23) Trasatti, S. Work function, electronegativity, and electrochemical behaviour of metals: III. Electrilytic hydrogen evolution in acid solutions. *J. Electroanal. Chem. Interfacial Electrochem.* **1972**, *39*, 163−184.

(24) Dimeglio, J. L.; Rosenthal, J. Selective conversion of CO_2 to CO with high efficiency using an inexpensive bismuth-based electrocatalyst. *J. Am. Chem. Soc.* **2013**, *135*, 8798−8801.

(25) Medina-Ramos, J.; Dimeglio, J. L.; Rosenthal, J. Efficient reduction of CO_2 to CO with high current density using in situ or ex situ prepared Bi-Based materials. *J. Am. Chem. Soc.* **2014**, *136*, 8361−8367.

(26) Atifi, A.; Keane, T. P.; DiMeglio, J. L.; Pupillo, R. C.; Mullins, D. R.; Lutterman, D. A.; Rosenthal, J. Insights into the composition and function of a bismuth-based catalyst for reduction of CO_2 to CO. *J. Phys. Chem. C* **2019**, *123*, 9087−9095.

(27) Zhang, Z. Y.; Chi, M. F.; Veith, G. M.; Zhang, P. F.; Lutterman, D. A.; Rosenthal, J.; Overbury, S. H.; Dai, S.; Zhu, H. Y. Rational design of Bi nanoparticles for efficient electrochemical CO_2 reduction:

the elucidation of size and surface condition effects. *ACS Catal.* **2016**, *6*, 6255−6264.
(28) García de Arquer, F. P.; Bushuyev, O. S.; De Luna, P.; Dinh, C. T.; Seifitokaldani, A.; Saidaminov, M. I.; Tan, C. S.; Quan, L. N.; Proppe, A.; Kibria, M. G.; Kelley, S. O.; Sinton, D.; Sargent, E. H. 2D metal oxyhalide-derived catalysts for effcient CO_2 electroreduction. *Adv. Mater.* **2018**, *30*, 1802858.
(29) Yang, H.; Han, N.; Deng, J.; Wu, J. H.; Wang, Y.; Hu, Y. P.; Ding, P.; Li, Y. F.; Li, Y. G.; Lu, J. Selective CO_2 reduction on 2D mesoporous Bi nanosheets. *Adv. Energy Mater.* **2018**, *8*, 1801536.
(30) Fan, L.; Xia, Z.; Xu, M. J.; Lu, Y. Y.; Li, Z. J. 1D SnO_2 with wire-in-tube architectures for highly selective electrochemical reduction of CO_2 to C_1 products. *Adv. Funct. Mater.* **2018**, *28*, 1706289.
(31) Han, N.; Wang, Y.; Yang, H.; Deng, J.; Wu, J. H.; Li, Y. F.; Li, Y. G. Ultrathin bismuth nanosheets from in situ topotactic transformation for selective electrocatalytic CO_2 reduction to formate. *Nat. Commun.* **2018**, *9*, 1320.
(32) Qin, Y.; Lee, S. M.; Pan, A. L.; Gösele, U.; Knez, M. Rayleigh-instability-induced metal nanoparticle chains encapsulated in nanotubes produced by atomic layer deposition. *Nano Lett.* **2008**, *8*, 114−118.
(33) Zhang, E.; Wang, T.; Yu, K.; Liu, J.; Chen, W. X.; Li, A.; Rong, H. P.; Lin, R.; Ji, S. F.; Zheng, X. S.; Wang, Y.; Zheng, L. R.; Chen, C.; Wang, D. S.; Zhang, J. T.; Li, Y. D. Bismuth single atoms resulting from transformation of metal-organic frameworks and their use as electrocatalysts for CO_2 reduction. *J. Am. Chem. Soc.* **2019**, *141*, 16569−16573.
(34) Wu, J. J.; Yadav, R. M.; Liu, M. J.; Sharma, P. P.; Tiwary, C. S.; Ma, L. L.; Zou, X. L.; Zhou, X. D.; Yakobson, B. I.; Lou, J.; Ajayan, P. M. Achieving highly efficient, selective, and stable CO_2 reduction on nitrogen-doped carbon nanotubes. *ACS Nano* **2015**, *9*, 5364−5371.
(35) Han, N.; Wang, Y. Y.; Deng, J.; Zhou, J. H.; Wu, Y. L.; Yang, H.; Ding, P.; Li, Y. G. Self-templated synthesis of hierarchical mesoporous SnO_2 nanosheets for selective CO_2 reduction. *J. Mater. Chem. A* **2019**, *7*, 1267−1272.
(36) Gong, Q. F.; Ding, P.; Xu, M. Q.; Zhu, X. R.; Wang, M. Y.; Deng, J.; Ma, Q.; Han, N.; Zhu, Y.; Lu, J.; Feng, Z. X.; Li, Y. F.; Zhou, W.; Li, Y. G. Structural defects on converted bismuth oxide nanotubes enable highly active electrocatalysis of carbon dioxide reduction. *Nat. Commun.* **2019**, *10*, 2807.
(37) Koh, J. H.; Won, D. H.; Eom, T.; Kim, N. K.; Jung, K. D.; Kim, H. J.; Hwang, Y. J.; Min, B. K. Facile CO_2 electro-reduction to formate via oxygen bidentate intermediate stabilized by high-index planes of Bi dendrite catalyst. *ACS Catal.* **2017**, *7*, 5071−5077.
(38) Ugarte, D.; Chatelain, A.; de Heer, W. A. Nanocapillarity and chemistry in carbon nanotubes. *Science* **1996**, *274*, 1897−1899.
(39) Regan, B. C.; Aloni, S.; Ritchie, R. O.; Dahmen, U.; Zettl, A. Carbon nanotubes as nanoscale mass conveyors. *Nature* **2004**, *428*, 924−927.
(40) Kim, B. M.; Sinha, S.; Bau, H. H. Optical microscope study of liquid transport in carbon nanotubes. *Nano Lett.* **2004**, *4*, 2203−2208.
(41) Majumder, M.; Chopra, N.; Andrews, R.; Hinds, B. Nanoscale hydrodynamics: enhanced flow in carbon nanotubes. *Nature* **2005**, *438*, 930.
(42) Ma, L. B.; Zhang, W. J.; Wang, L.; Hu, Y.; Zhu, G. Y.; Wang, Y. R.; Chen, R. P.; Chen, T.; Tie, Z. X.; Liu, J.; Jin, Z. Strong capillarity, chemisorption, and electrocatalytic capability of crisscrossed nanostraws enabled flexible, high-rate, and long-cycling lithium-sulfur batteries. *ACS Nano* **2018**, *12*, 4868−4876.
(43) Pan, X. L.; Bao, X. H. The effects of confinement inside carbon nanotubes on catalysis. *Acc. Chem. Res.* **2011**, *44*, 553−562.
(44) Bertin, E.; Garbarino, S.; Roy, C.; Kazemi, S.; Guay, D. Selective electroreduction of CO_2 to formate on Bi and oxide-derived Bi films. *J. CO2 Utilization* **2017**, *19*, 276−283.
(45) Zhang, W. J.; Hu, Y.; Ma, L. B.; Zhu, G. Y.; Zhao, P. Y.; Xue, X. L.; Chen, R. P.; Yang, S. Y.; Ma, J.; Jin, Z.; Liu, J. Liquid-phase exfoliated ultrathin Bi nanosheets: uncovering the origins of enhanced electrocatalytic CO_2 reduction on two-dimensional metal nanostructure. *Nano Energy* **2018**, *53*, 808−816.
(46) Zhang, Y.; Zhang, X. L.; Ling, Y. Z.; Li, F. W.; Bond, A. M.; Zhang, J. Controllable synthesis of few-layer bismuth subcarbonate by electrochemical exfoliation for enhanced CO_2 reduction performance. *Angew. Chem., Int. Ed.* **2018**, *57*, 13283−13287.
(47) Tran-Phu, T.; Daiyan, R.; Fusco, Z.; Ma, Z. P.; Amal, R.; Tricoli, A. Nanostructured β-Bi_2O_3 fractals on carbon fibers for highly selective CO_2 electroreduction to formate. *Adv. Funct. Mater.* **2020**, *30*, 1906478.
(48) Liu, S. B.; Xiao, J.; Lu, X. F.; Wang, J.; Wang, X.; Lou, X. W. Efficient electrochemical reduction of CO_2 to HCOOH over sub-2 nm SnO_2 quantum wires with exposed grain boundaries. *Angew. Chem., Int. Ed.* **2019**, *58*, 8499−8503.
(49) Li, F. W.; Xue, M. Q.; Li, J. Z.; Ma, X. L.; Chen, L.; Zhang, X. J.; Macfarlane, D. R.; Zhang, J. Unlocking the electrocatalytic activity of antimony for CO_2 reduction by two-dimensional engineering of the bulk material. *Angew. Chem., Int. Ed.* **2017**, *56*, 14718−14722.
(50) Zouaoui, N.; Ossonon, B. D.; Fan, M. Y.; Mayilukila, D.; Garbarino, S.; de Silveira, G.; Botton, G. A.; Guay, D.; Tavares, A. C. Electroreduction of CO2 to formate on amine modified Pb electrodes. *J. Mater. Chem. A* **2019**, *7*, 11272−11281.
(51) Zhang, Z. R.; Ahmad, F.; Zhao, W. H.; Yan, W. S.; Zhang, W. H.; Huang, H. W.; Ma, C.; Zeng, J. Enhanced electrocatalytic reduction of CO_2 via chemical coupling between indium oxide and reduced graphene oxide. *Nano Lett.* **2019**, *19*, 4029−4034.
(52) Min, S. X.; Yang, X. L.; Lu, A.; Tseng, C.; Hedhili, M. N.; Li, L.; Huang, K. Low overpotential and high current CO_2 reduction with surface reconstructed Cu foam electrodes. *Nano Energy* **2016**, *27*, 121−129.

https://dx.doi.org/10.1021/acs.nanolett.1c00390
Nano Lett. 2021, 21, 2650−2657